

ASPERA-3: Analyser of Space Plasmas and Energetic Ions for Mars Express

S. Barabash¹, R. Lundin¹, H. Andersson¹, J. Gimholt^{1,a}, M. Holmström¹, O. Norberg^{1,b}, M. Yamauchi¹, K. Asamura², A.J. Coates³, D.R. Linder³, D.O. Kataria³, C.C. Curtis⁴, K.C. Hsieh⁴, B.R. Sandel⁴, A. Fedorov^{5,c}, A. Grigoriev^{5,d}, E. Budnik^{5,c}, M. Grande⁶, M. Carter⁶, D.H. Reading⁶, H. Koskinen⁷, E. Kallio⁷, P. Riihela⁷, T. Säles⁷, J. Kozyra⁸, N. Krupp⁹, S. Livi^{9,e}, J. Woch⁹, J. Luhmann¹⁰, S. McKenna-Lawlor¹¹, S. Orsini¹², R. Cerulli-Irelli¹², M. Maggi¹², A. Morbidini¹², A. Mura¹², A. Milillo¹², E. Roelof¹³, D. Williams¹³, J.-A. Sauvaud¹⁴, J.-J. Thocaven¹⁴, T. Moreau¹⁴, D. Winningham¹⁵, R. Frahm¹⁵, J. Scherrer¹⁵, J. Sharber¹⁵, P. Wurz¹⁶ & P. Bochsler¹⁶

¹*Swedish Institute of Space Physics, Box 812, S-98 128, Kiruna, Sweden*

Email: stas@irf.se

²*Institute of Space and Astronautical Science, 3-1-1 Yoshinodai, Sagamichara, Japan*

³*Mullard Space Science Laboratory, University College London, Surrey RH5 6NT, UK*

⁴*University of Arizona, Tucson, AZ 85721, USA*

⁵*Space Research Institute, 117810 Moscow, Russia*

⁶*Rutherford Appleton Laboratory, Chilton, Didcot, Oxfordshire OX11 0QX, UK*

⁷*Finnish Meteorological Institute, Box 503 FIN-00101 Helsinki, Finland*

⁸*Space Physics Research Laboratory, University of Michigan, Ann Arbor, MI 48109-2143, USA*

⁹*Max-Planck-Institut für Aeronomie, D-37191 Katlenburg-Lindau, Germany*

¹⁰*Space Science Laboratory, University of California in Berkeley, Berkeley, CA 94720-7450, USA*

¹¹*Space Technology Ltd., National University of Ireland, Maynooth, Co. Kildare, Ireland*

¹²*Instituto di Fisica dello Spazio Interplanetari, I-00133 Rome, Italy*

¹³*Applied Physics Laboratory, Johns Hopkins University, Laurel, MD 20723-6099, USA*

¹⁴*Centre d'Etude Spatiale des Rayonnements, BP-4346, F-31028 Toulouse, France*

¹⁵*Southwest Research Institute, San Antonio, TX 7228-0510, USA*

¹⁶*University of Bern, Physikalisches Institut, CH-3012 Bern Switzerland*

^a*now at Scania, Volvo Corporation, Södertälje, Sweden*

^b*now at ESRANGE, Swedish Space Corporation, Kiruna, Sweden*

^c*now at Centre d'Etude Spatiale des Rayonnements, Toulouse, France*

^d*now at Swedish Institute of Space Physics, Box 812, S-981 28 Kiruna, Sweden*

^e*now at Applied Physics Laboratory, Johns Hopkins University, Laurel, MD 20723, USA*

The ASPERA-3 (Analyser of Space Plasma and Energetic Atoms) instrument of Mars Express is designed to study the solar wind-Mars atmosphere interaction and to characterise the plasma and neutral gas environment in near-Mars space through energetic neutral atom (ENA) imaging and local charged-particle measurements. The studies address the fundamental question: how strongly do the interplanetary plasma and electromagnetic fields affect the martian atmosphere? This question is directly related to the problem of martian dehydration. The instrument comprises four sensors; two ENA sensors, and electron and ion spectrometers. The Neutral Particle Imager (NPI) measures the integral ENA flux (0.1-60 keV) with no mass and energy resolution but with high angular resolution. The Neutral Particle Detector (NPD) measures the ENA flux, resolving energy (0.1-10 keV) and mass (H and O) with a coarse angular resolution. The electron spectrometer (ELS) is a standard top-hat electrostatic analyser of a very compact design. These three sensors are mounted on a scanning platform providing 4π coverage. The instrument includes an ion mass composition sensor, IMA (Ion Mass Analyser). Mechanically, IMA is a separate unit connected by a cable to the ASPERA-3 main unit. IMA provides ion measurements in the energy range 0.01-40 keV/ q for the main ion components H^+ , He^{2+} , He^+ , O^+ , with 20-80 amu/ q .

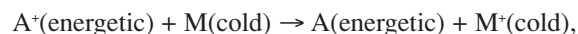
1. The Science

1.1 Scientific task

The scientific objectives of the Mars Express Orbiter mission are to study the subsurface, surface and atmosphere of Mars, as well as the interaction of the atmosphere with the interplanetary medium. ASPERA-3 will fulfil the last objective by:

- remote measurements of energetic neutral atoms (ENAs) in order to (a) investigate the interaction between the solar wind and the martian atmosphere, (b) characterise quantitatively the impact of plasma processes on atmospheric evolution, and (c) obtain the global plasma and neutral gas distributions in the near-Mars environment;
- *in situ* measurements of ions and electrons to (a) complement the ENA images (electrons and multi-charged ions cannot be imaged), (b) study local characteristics of the plasma (dynamics and fine structure of boundaries), (c) provide the undisturbed solar wind parameters required for interpreting ENA images.

As established by earlier missions, and confirmed recently by Mars Global Surveyor, Mars does not possess an intrinsic dipole magnetic field but only local crustal magnetisations (Acuna et al., 1998). The local field plays a role in the solar wind interaction only over limited regions. For the overall interaction picture, the solar wind interacts directly with the martian ionosphere, exosphere and upper atmosphere. As a result of the low gravity on Mars, the neutral density can reach 10^4 - 10^6 cm $^{-3}$ in the interaction region where the main plasma boundaries, bow shock and magnetopause, are located. The co-existence of these two components, the solar wind plasma and the planetary neutral gas, produces a strong interaction. One of the fundamental collisional interactions is the charge-exchange process between the energetic ion, A^+ , and the cold atmospheric gas, M :



which produces energetic neutral atoms, A , and an ionised gas particle. Directional detection of the ENA thereby yields a global image of the interaction, if the observer is at a remote location with respect to the plasma population (Wurz, 2000). ASPERA-3 will concentrate on studying the effects of the plasma-neutral coupling at Mars via ENA imaging, complemented by the electron and ion observations.

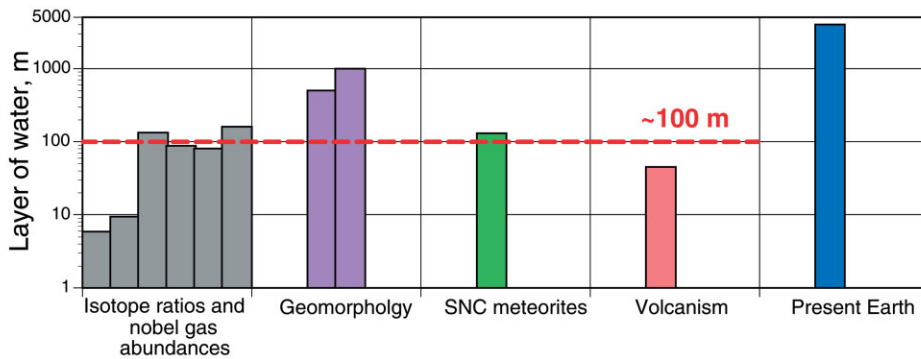


Fig. 1. Martian water inventory derived from different approaches. The present Earth is also shown for reference (adapted from McKay & Stoker, 1989).

1.2 The solar wind-atmosphere coupling

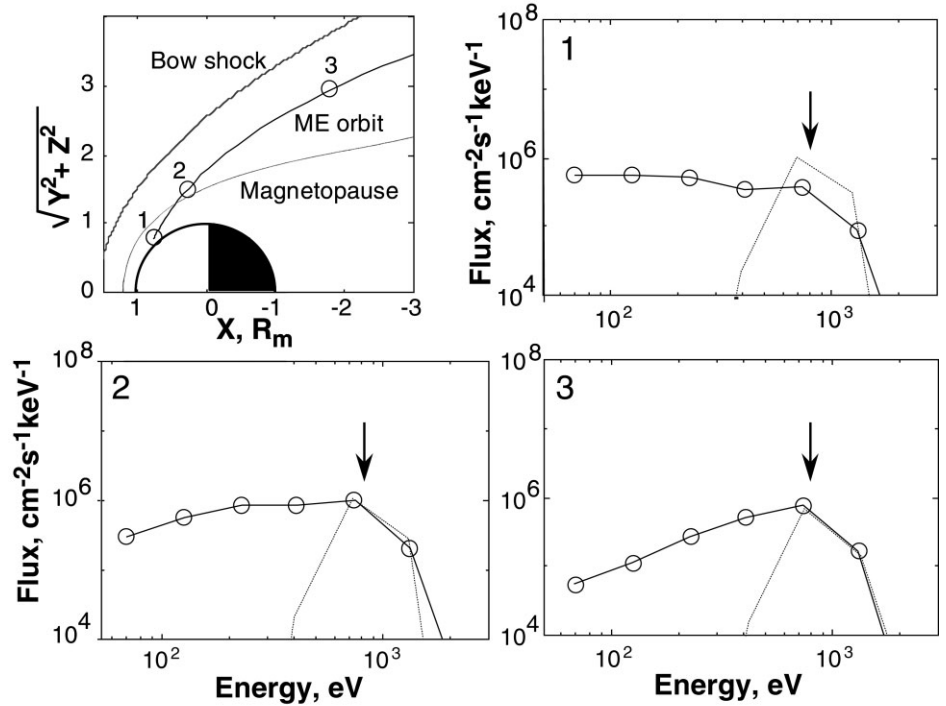
Near-Mars space is strikingly different from Earth-space because of the absence of a substantial intrinsic martian magnetic field. Without the magnetic cavity of a magnetosphere to shield the upper atmosphere from the solar wind, Mars is subject to comet-like atmosphere erosion processes and solar wind-induced current systems that have no terrestrial counterparts. From previous missions to Mars (especially Phobos-2) and from Pioneer Venus Orbiter circling the similarly weakly magnetised Venus, ideas on how the martian upper atmosphere and solar wind interact and the consequences for the planet have been developed. In particular, the scavenging of planetary ions may have resulted in the removal of ~ 1 m of surface water over 4.5 Gyr (Lundin et al., 1991). More detailed studies (Perez-de-Tejada, 1992), taking into account the variability of the ionosphere throughout the planet's history, give a much higher (~ 30 m) equivalent depth of water that has escaped owing to the solar wind interaction process.

The current atmospheric conditions on Mars indicate that water does not exist on the surface in any significant amount: 15 mm equivalent water layer (Farmer et al., 1977). On the other hand, independent analyses of several features of the planet unambiguously indicate that water did exist in the past on the martian surface. Fig. 1 shows the water inventory based on different approaches: geomorphologic features, analysis of the SNC meteorites, isotopic abundance and volcanic activity. The total amount of past surface water results in an equivalent water layer of at least 100 m. This leads to the problem of martian dehydration. Where is the water? Is it lost or frozen and buried? If the former, what could produce such an effective escape mechanism? If the latter, where is this tremendous amount of water stored? As indicated above, the processes associated with the solar-wind interaction could account for the escape of up to 30% of past surface water.

Another problem of the solar wind-atmosphere coupling that has not been explored experimentally is the energetic consequences for the atmosphere of the lack of a significant dipole field. Kinetic and test-particle models of the Mars-solar wind interaction (Brecht, 1997; Kallio et al., 1997) suggest that solar wind absorption by the atmosphere may be an important energy source for the upper atmosphere. The ENAs generated as a product of the solar wind interaction increase the deposition of solar wind energy (Kallio & Barabash, 2001) and, at the same time, provide a means of 'imaging' the solar wind interaction. The atmosphere, although thin, alters the incoming energetic solar wind by:

- generation of ionospheric currents that partially deflect the ion flow around the ionosphere;
- 'mass loading' the solar wind with planetary ions produced mainly by photoionisation, and solar wind electron impact ionisation of the atmospheric gases;
- undergoing charge-transfer or charge-exchange interactions with the solar wind ions.

Fig. 2. ENA spectra along the Mars Express orbit. The ENAs originate in the shocked solar wind. The arrows mark ENA flux produced in the upstream solar wind. The energy resolution corresponds to that of ASPERA-3.



According to the models, some of the solar wind ions (mainly protons and alpha particles) directly impact Mars' upper atmosphere near its exobase (~ 180 km altitude) because their gyroradii are too large to behave as a deflected 'fluid' in the subsolar magnetosheath (Brecht, 1997; Kallio & Janhunen, 2001) or because they are partially thermalised by the bow shock (Kallio et al., 1997). Others undergo charge-exchange reactions with ambient exospheric and thermospheric neutrals, particularly hydrogen, and then impact the exobase as ENAs (Kallio et al., 1997). In both cases, solar wind energy is 'directly' deposited into the upper atmosphere, increasing ionisation rates and UV emissions. Kallio & Barabash (2000, 2001) have studied the effects of such ENA precipitation using Monte Carlo simulations and estimated that, under typical solar wind conditions, the precipitating hydrogen atoms increase the ionisation rate by about 1% in comparison with ionisation rates owing to extreme UV radiation. This effect is comparable to, or even stronger than, similar effects caused by the O^+ and H^+ precipitation (Luhmann & Kozyra, 1991; Brecht, 1997; Kallio & Janhunen, 2001). The results also indicate that a substantial part of the incoming particles is scattered back from the atmosphere, resulting in an ENA hydrogen albedo. Imaging these particles would visualise the spots or regions of the most intense ENA precipitation.

While the energy transfer associated with the proton or ENA precipitation exceeds that from the O^+ precipitation, it is the oxygen ions that cause massive sputtering of the atmosphere (Luhmann & Kozyra, 1991; Luhmann et al., 1992). Luhmann & Bauer (1992) estimated that the O^+ sputtering results in the escape of 0.1 - 0.5 $kg\ s^{-1}$ of oxygen atoms. This is on the same level as the non-thermal escape of the hot oxygen atmospheric component. For comparison, the direct solar wind pick-up, excluding the bulk ionospheric scavenging, removes 0.01 $kg\ s^{-1}$ at most.

1.3 Sources of energetic neutral atoms at Mars

Barabash et al. (1995), Kallio et al. (1997), Holmström et al. (2002), Mura et al. (2002), Lichtenegger et al. (2002) and Barabash et al. (2002) considered the ENA production at Mars. ENAs are produced by charge-exchange between the exosphere containing H, H_2 , He and O, and the different plasma populations such as:

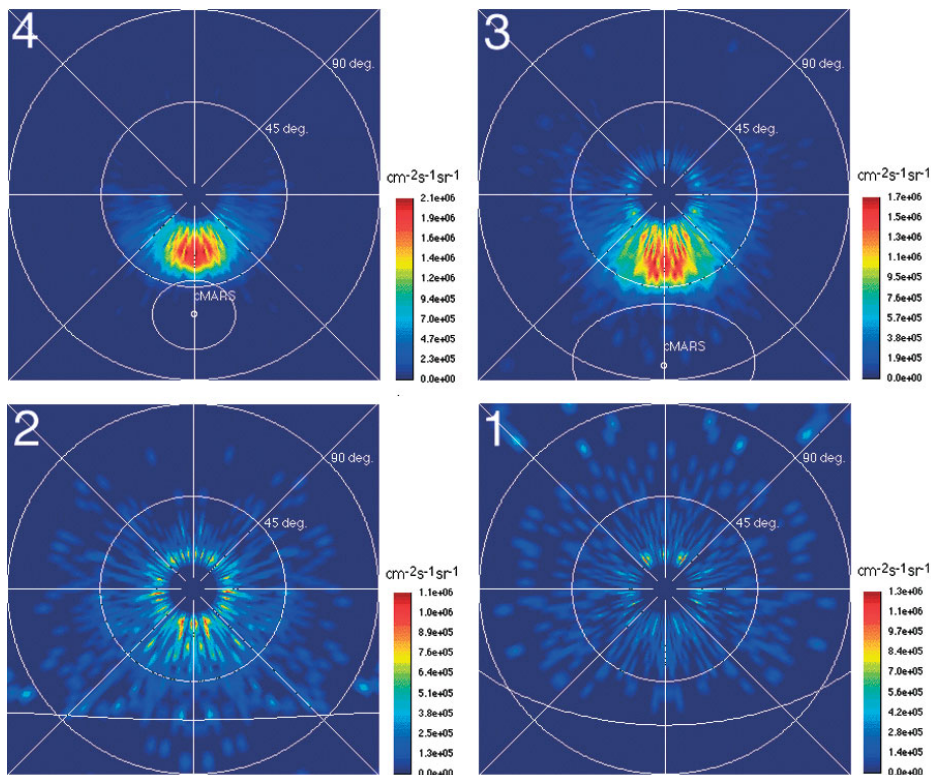


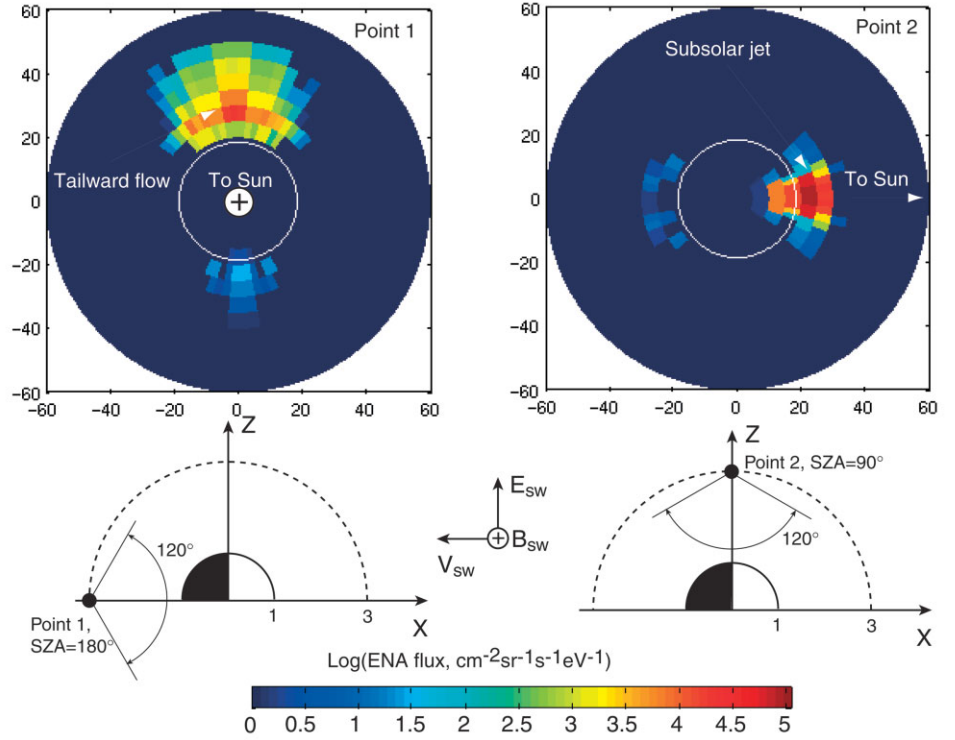
Fig. 3. Model ENA images for four locations along the Mars Express orbit (three marked in the inset of Fig. 2); position 4 (not shown in Fig. 2) corresponds to the orbit apocentre. The polar axis looks towards the Sun. The polar angle is the azimuth at the vantage point and the radius is the polar angle to the Sun direction. The solar wind ENAs are blocked.

- the supersonic solar wind (Holmström et al., 2002);
- the shocked solar wind (Holmström et al., 2002);
- accelerated planetary ions (Barabash et al., 2002; Lichtenegger et al., 2002);
- the tiny Phobos atmosphere can also interact with both the supersonic and the shocked solar wind, resulting in ENA generation (Mura et al., 2002);
- the energetic O^+ ions picked up by the plasma flow incident on the atmosphere are backscattered and sputter oxygen, CO_2 and its fragments (Luhmann & Kozyra, 1991; Luhmann et al., 1992). The backscattered and sputtered atoms have energies up to few hundred eV and form an oxygen ENA albedo. The intensity of these emissions directly determines the efficiency of the atmospheric erosion;
- the precipitating protons and hydrogen ENAs can also be scattered back, forming a hydrogen ENA albedo (Kallio & Barabash, 2001; Holmström et al., 2002).

The supersonic solar wind upstream of the bow shock can experience charge-exchange with the hydrogen exosphere over very long distances, producing a narrow ($\approx 10^\circ$) anti-Sunward beam of ENAs with the energy of the bulk flow of the solar wind (the spectrum marked by arrows in Fig. 2). These ENAs can be detected only at the beam edges because they are superimposed on the intense flux of the solar radiation.

The shocked solar wind is the strongest source of ENAs because the protons flowing around Mars can interact with dense neutral gas. The detailed modelling of the ENA production from this source was performed by Kallio et al. (1997), Holmström et al. (2002) and Mura et al. (2002). Using these models, ENA images that would be observed from the Mars Express orbit were simulated for solar maximum conditions. The spacecraft will reach Mars during the moderate solar activity characteristic of the decline of the solar cycle. The ENA emissions are weaker during solar maximum so the calculations give lower limits for the ENA fluxes. Fig. 2 shows the ENA spectra integrated over the unit sphere for several locations along the Mars

Fig. 4. Model ENA images of the pick-up oxygen ions for two vantage points in the tail and at the pole. The vantage points are in the plane perpendicular to the ecliptic. The polar axis is towards the planetary centre. The image projection is similar to that of Fig. 3. The energy range is 0.1-1.65 keV. The electric and magnetic field vectors in the solar wind are shown for reference.



Express orbit. The estimated ENA fluxes are well above $10^4 \text{ cm}^{-2} \text{ s}^{-1} \text{ keV}^{-1}$ and, therefore, easily detectable. The directional fluxes to be measured well exceed $10^5 \text{ cm}^{-2} \text{ s}^{-1} \text{ sr}^{-1}$.

Fig. 3 shows the directional ENA flux integrated over energy as a function of two spherical angles (ENA images) for several positions along the Mars Express orbit marked in Fig. 2. Position 4 corresponds to the apocentre. In this fish-eye projection, the polar axis is looking towards the Sun. The polar angle is the azimuth at the vantage point and the radius is the polar angle to the Sun direction. The images display the entire interaction region and can be converted into global distributions of the proton flow and neutral gas using extracting diagnostic methods similar to that developed for the Earth's conditions (Roelof & Skinner, 2000). Holmström et al. (2002) showed that the ENA fluxes generated from the shocked solar wind are most sensitive to the neutral hydrogen distribution controlled by the exobase temperature and the position of the boundary separating the solar wind and planetary plasmas.

Some of the ENAs produced by the shocked solar wind and ENAs originating in the solar wind can precipitate onto the ionosphere. Fig. 2 (position 1 inside the magnetosphere) gives a typical spectrum of precipitating ENAs at the 45° solar zenith angle. The spectrum is rather flat at the level $7 \times 10^5 \text{ cm}^{-2} \text{ s}^{-1} \text{ keV}^{-1}$. The peak corresponds to the solar wind energy. The planetary protons originating from ionisation of the hydrogen corona can charge-exchange with the exospheric gas as well, resulting in planetary hydrogen ENA emissions. These emissions, investigated in detail by Lichtenegger et al. (2002), differ from the shocked solar wind ENAs in energy because the pick-up protons can gain an energy up to four times that of the solar wind.

The ASPERA/Phobos observations of the plasma energisation inside the martian magnetosphere (Lundin et al., 1993) showed the existence of two basic ion populations: the tail beams of H^+ and O^+ of energy 1-3 keV, and outflowing ionospheric ions of energy 10-100 eV near the tail flanks. Barabash et al. (1995) estimated the related ENA flux to be $10^3 \text{ cm}^{-2} \text{ s}^{-1} \text{ keV}^{-1}$ for the energy range 1-10 keV, and up to $10^5 \text{ cm}^{-2} \text{ s}^{-1} \text{ keV}^{-1}$ for 10-100 eV. The ENA signal associated with the pick-up oxygen was investigated in detail by Barabash et al. (2002). Using the

empirical model of the solar wind plasma flow near Mars developed by Kallio & Koskinen (1999), Barabash et al. (2002) numerically solved the kinetic equation and obtained the global distribution of oxygen ions. This distribution was then converted to the corresponding ENA flux. It was found that the fluxes of the oxygen ENAs could reach $10^4 \text{ cm}^{-2} \text{ s}^{-1} \text{ keV}^{-1}$ and fully reflect the morphology of the oxygen population. This provides a way to determine the instantaneous oxygen escape rate. One of the simulated images for the energy range 0.1-1.65 keV is reproduced in Fig. 4. The projection is similar to that used for hydrogen ENA images but the polar axis in the vantage point points towards the centre of the planet. The image shows a strong ENA jet from the subsolar point, where the electric and magnetic field configuration effectively accelerates newborn planetary ions. The tailward flow is also clearly reproduced. The corresponding vantage points are shown below the images.

Several experiments on the Phobos mission observed brief plasma disturbances when the spacecraft crossed that moon's orbit (Barabash, 1995). They could be related to a hypothetical neutral gas torus resulting from the moon outgassing. The solar wind plasma can experience charge-exchange with the Phobos 'atmosphere' and the neutral torus, resulting in ENA emissions. Assuming an outgassing rate of 10^{23} s^{-1} , Mura et al. (2002) calculated the associated ENA flux to be of the order of 10^3 - $10^4 \text{ cm}^{-2} \text{ s}^{-1} \text{ keV}^{-1}$ for the shocked solar wind plasma, and up to $10^6 \text{ cm}^{-2} \text{ s}^{-1} \text{ keV}^{-1}$ for the solar wind beam. Because of solar radiation, the Phobos ENAs and the Phobos torus ENAs can be observed only when the moon is in the magnetosheath and the plasma flow deviates strongly from the anti-solar direction.

1.4 ENA imaging of the martian environment

ASPERA-3 will image all of the above ENA sources. The images provide two-fold information. Firstly, they reveal morphological features of the ENA sources, such as the location of boundaries and their relative sizes. ENA images are useful, in particular, for investigating different types of asymmetries expected for the plasma flow near Mars (Dubinin et al., 1996). The ENA images of the escaping plasma display globally and instantaneously the size and geometry of the outflowing plasma region. These characteristics are particularly important for calculations of the total non-thermal plasma outflow. For instance, the local ion measurements made using the ASPERA and TAUS instruments during the Phobos mission gave comparable ion fluxes. However, different assumptions made regarding the outflow region geometry (mass-loading boundary, plasma sheet) resulted in significant differences in the total outflow rate estimations, 0.5 - 1.0 kg s^{-1} (Lundin et al., 1989) and 0.15 kg s^{-1} (Verigin et al., 1991). One of the reasons for this was ambiguity in separating spatial and temporal variations, which is typical for local plasma measurements. Global and instantaneous observations of the outflowing plasma region morphology to be made via ENA imaging would help to resolve this issue, which is important for understanding the planetary atmosphere evolution.

Secondly, ENA images carry ample quantitative information about both the planetary plasma and neutral environments. By applying extraction techniques to the images of the shocked solar wind, quantitative models will be obtained giving the neutral gas profiles (exobase densities and temperatures) and global proton plasma distributions (flow geometry, bulk velocity, density and temperature).

Aerobraking measurements from Mars Global Surveyor (Dornheim, 1997) indicate that the atmospheric density at 150 km altitude varies by 30% in one out of three passes. Estimated scale heights of $\sim 8 \text{ km}$ implies that the densities in the interaction region higher up will also be much more variable with time than had been expected. Global ENA imaging of the interaction offers the greatest promise of separating the spatial and temporal variations of the atmosphere-solar wind interaction. Apart from imaging, the measurements of ENA flux from certain directions provide a diagnostic tool for plasma-atmosphere coupling studies. Precipitating ENAs and ENA albedo (backscattered oxygen) are direct manifestations of such an interaction.

Table 1. ASPERA-3 scientific objectives.		
<i>Scientific objective</i>	<i>Associated Measurements</i>	<i>Measurement Requirements</i>
Determine the instantaneous global distributions of plasma and neutral gas near the planet	ENAs originating from the shocked solar wind	Measure the ENA flux in the energy range tens eV - few keV with 4π coverage. ENA flux $>10^4 \text{ cm}^{-2} \text{ s}^{-1} \text{ keV}^{-1}$. Measure the upstream solar wind parameters
Study plasma-induced atmospheric escape	ENAs originating from inside the magnetosphere	Mass-resolving (H/O) ENA measurements in the energy range up to tens keV. ENA flux $>10^9 \text{ cm}^{-2} \text{ s}^{-1} \text{ keV}^{-1}$
Investigate the modification of the atmosphere through ion bombardment	ENA albedo	Mass-resolving (H/O) ENA measurements in the energy range down to tens eV from the nadir direction. ENA flux $>10^9 \text{ cm}^{-2} \text{ s}^{-1} \text{ keV}^{-1}$ (100 eV)
Investigate the energy deposition from the solar wind to the ionosphere	Precipitating ENAs	ENA measurements in the energy range tens eV - few keV. ENA flux $>10^4 \text{ cm}^{-2} \text{ s}^{-1} \text{ keV}^{-1}$
Search for the solar wind-Phobos interactions	ENA originating from Phobos	ENA measurements in the energy range tens eV - few keV with 4π coverage. ENA flux $10^4 \text{ cm}^{-2} \text{ s}^{-1} \text{ keV}^{-1}$
Define the local characteristics of the main plasma regions	Ion and electron measurements of hot plasma	Ion and electron measurements in the energy range few eV - tens keV with 4π coverage

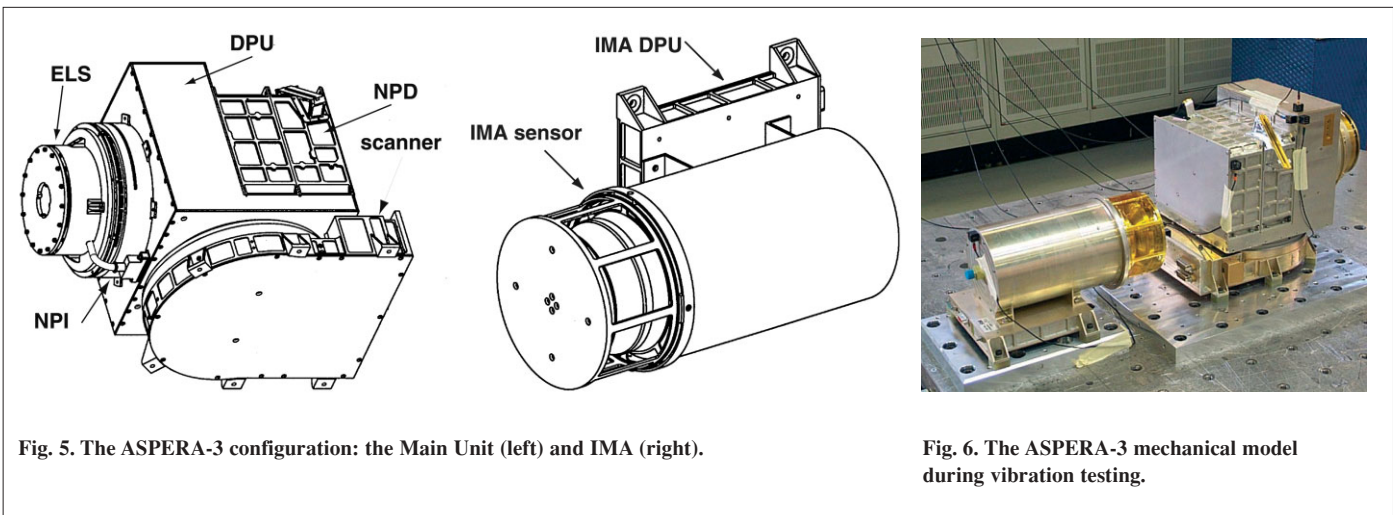


Fig. 5. The ASPERA-3 configuration: the Main Unit (left) and IMA (right).

Fig. 6. The ASPERA-3 mechanical model during vibration testing.

1.5 Scientific objectives and measurements requirements

The studies of martian ENAs resulting from the solar wind-atmosphere interaction address the fundamental question: how strongly do the interplanetary plasma and electromagnetic fields affect the atmosphere? This question is directly related to the problem of martian dehydration as described in Section 1.2. What happened to the martian water that once flowed in numerous channels? As we know from terrestrial experience, together with an inventory of organic compounds and external energy sources, liquid water is a fundamental requirement for life as we know it. Therefore, a clear understanding of the fate of the martian water is crucial for resolving whether life has ever existed on Mars.

The general scientific task of studying the solar wind-atmosphere interaction through ENA imaging can be subdivided into specific scientific objectives. These are listed in Table 1, together with the corresponding instrument requirements.

1.6 Relation to other missions

ASPERA-3 will perform the first ENA imaging of another planet in the low energy

range. No instruments with similar scientific objectives and capabilities are foreseen to fly to other planets. The only similar experiment, ASPERA-C, was carried by the failed Mars-96 mission. However, it did not have the ENA energy-analysing Neutral Particle Detector.

2.1 Overview

ASPERA-3 is designed for the analysis of ENAs, electrons and ions, with complete spherical coverage. Mechanically, ASPERA-3 (Figs. 5 and 6) consists of two units, the Main Unit (MU) and the Ion Mass Analyser (IMA). The MU comprises three sensors: NPI, NPD and ELS, with a digital processing unit, all located on a scan platform. All mechanical and electrical interfaces are made through the scan platform. The instrument's total mass is 8.2 kg and its power consumption 13.5 W. The MU envelope is 359x393x234 mm, and for IMA 255x150x150 mm.

2.2 Measurement principles and capabilities

To fulfil its scientific objectives, ASPERA-3 comprises four sensors; two ENA sensors (NPI, NPD), an electron spectrometer (ELS) and an ion mass analyser (IMA). The two ENA sensors are optimised for some of the scientific objectives, while being complementary. This approach offers the necessary redundancy as well as the independent cross-checking necessary for such ground-breaking measurements at another planet. The charged particle sensors not only characterise the local plasma environment but also support ENA measurements in terms of charged particles background and inter-calibrations.

The Neutral Particle Imager measures the integral ENA flux with no mass and energy resolution but with $5 \times 11^\circ$ angular resolution. The intrinsic field of view is $9 \times 344^\circ$. The sensor uses a graphite surface to suppress the UV background. ENAs incident on the surface at a grazing angle of 20° are reflected and/or cause ion sputtering. A micro-channel plate (MCP) stack detects the reflected particles and sputtered fragments with a discrete anode. The NPI head is a replica of the NPI-MCP sensor developed for ASPERA-C on Mars-96 (launch failure) and successfully flown on the Swedish Astrid microsatellite, launched in 1995 (C:son Brandt et al., 2000).

The Neutral Particle Detector measures the ENA differential flux over the energy range 100 eV to 10 keV, resolving H and O with a coarse $5 \times 30^\circ$ angular resolution. The sensor consists of two identical detectors, each with a $9 \times 90^\circ$ intrinsic field of view. The measurement technique is based on a principle similar to that of NPI. ENAs incident on a surface at a grazing angle of 15° are reflected and generate secondary electron emission. The secondary electrons are transported to an MCP assembly, which gives the START signal. The reflected ENAs hit the second surface and again produce the secondary electrons used to generate the STOP signal. The time-of-flight (TOF) electronics give the ENA velocity. The pulse-height distribution analysis of the STOP signals provides a rough determination of the ENA mass.

The Electron Spectrometer measures electrons in the energy range 0.01-20 keV. The intrinsic field of view is $10 \times 360^\circ$. The 360° aperture is divided into 16 sectors. The sensor is a standard top-hat electrostatic analyser in a very compact design. ELS is a reduced version of the MEDUSA experiment for the Astrid-2 and Munin missions launched in 1998 and 2000 (Norberg et al., 2001).

The Ion Mass Analyser is an improved version of the ion mass spectrographs TICS/Freja, IMIS/Mars-96 and IMI/Nozomi (Norberg et al., 1998) and a copy of Rosetta's ICA instrument. The IMA sensor is a separate unit connected by a cable to ASPERA-3. It measures ions in the energy range $0.01-30 \text{ keV}/q$ for the main ion components H^+ , H^{2+} , He^+ , O^+ and for the group of molecular ions $20 < M/q < \sim 80$. Mechanically, IMA is a separate unit with a $4.6 \times 360^\circ$ field of view. Electrostatic sweeping performs elevation ($\pm 45^\circ$) coverage. The IMA sensor is a spherical electrostatic analyser followed by a circular magnetic separating section. A large-diameter MCP with a discrete anode images the matrix azimuth x mass.

NPI, NPD and ELS are mounted on a scanning platform. The combination of the

2. The Instrument

Table 2. Baseline performances of the NPI, NPD, ELS and IMA sensors.

<i>Parameter</i>	<i>NPI</i>	<i>NPD</i>	<i>ELS</i>	<i>IMA</i>
Particles to be measured	ENA	ENA	electrons	ions
Energy range, keV per charge	≈ 0.1 - 60	0.1 - 10	0.01 - 20	0.01 - 30
Energy resolution, $\Delta E/E$	No	0.8	0.08	0.07
Mass resolution	No	H, O	–	$m/q = 1, 2, 4, 8, 16, >20$
Intrinsic field of view	9 x 344°	9 x 180°	10 x 360°	90 x 360°
Angular resolution (FWHM)	4.6 x 11.5°	5 x 30°	10 x 22.5°	4.5 x 22.5°
G-factor*/ pixel, cm ² sr	2.5 x 10 ⁻³ (ϵ not incl.)	6.2 x 10 ⁻³ (ϵ not incl.)	5 x 10 ⁻⁴	3.5 x 10 ⁻⁴
Efficiency, ϵ , %	~ 1	0.1-20	inc. in G	inc. in G
Time resolution (full 3D), s	32	32	32	32
Mass, kg	0.7	1.3	0.3	2.2
Power, W	0.8	1.5	0.6	3.5

*G-factor is the instrument geometrical factor

360° field of view and the scans from 0° to 180° give the required 4π maximum coverage. The actual coverage depends on the instrument location on the spacecraft. Table 2 summarises the instrument performance.

2.3 Neutral Particle Imager (NPI)

The NPI head is a replica of the NPI-MCP sensor developed for ASPERA-C/Mars-96 and flown successfully on Astrid (Barabash, 1995). In NPI, the charged particles, electrons and ions are removed by the electrostatic deflection system, which consists of two discs separated by a 3 mm gap (Fig. 7). The 5 kV potential between the grounded and biased discs produces a strong electric field, which sweeps away all charged particles with energies up to 60 keV. Since the integral ENA flux substantially exceeds the charged particle flux for energies greater than 60 keV, this rejection energy provides satisfactory performance. The discs also collimate the incoming beam in the elevation angle. Apart from being ‘on’ or ‘off’, the deflection system can be operated in two other modes: ‘alternative’ and ‘sweeping’. In the alternative mode, the deflection system is turned on and off for one sampling time. This mode will be used for more accurate separation between charged and neutral particles entering the system. The deflection system is connected to the high-voltage supply via an optocoupler. Regulating the optocoupler reference voltage changes the deflection voltage performing the sweeping and alternating. In order to reduce the time for discharging the deflection system discs to 1 ms, a second parallel optocoupler is used.

The space between the deflection system discs is divided into 32 sectors by plastic spokes forming 32 azimuthal collimators with an aperture of 9x18° each. Neutrals passing through the deflection system hit a 32-sided conical target at a grazing angle of 20°. The interaction with the target generates secondary particles, both electrons and ions, and/or reflection of the primary neutrals. An MCP stack in a chevron configuration, followed by a 32-sector anode, detects the particles leaving the target. The signal from the MCP gives the direction of the primary incoming neutral. The MCP operates in ion mode with a negative bias of –2.6 kV applied to the front side and thus detects (a) sputtered positive ions of the target material, (b) positive ions resulting from ionisation of the primary neutrals, and (c) neutrals reflected from the target surface. In order to improve the angular resolution and collimate the particles leaving the interaction surface, 32 separating walls are attached to the target, forming

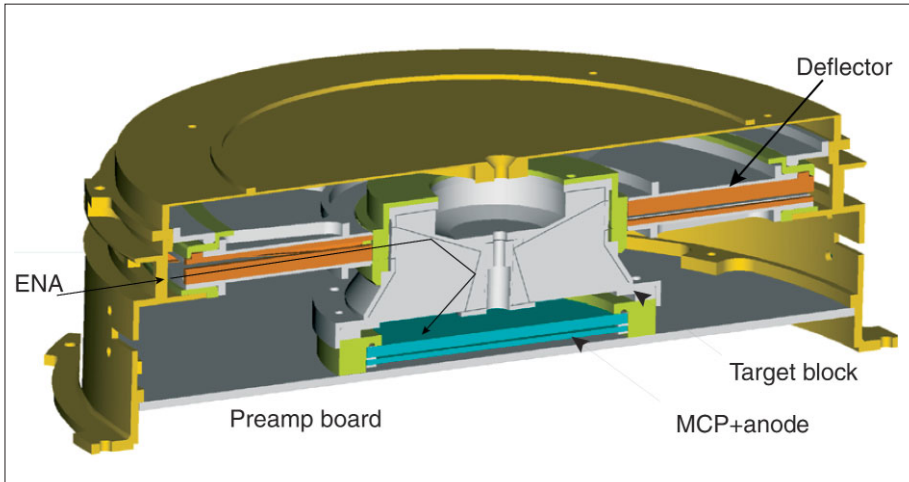


Fig. 7. Cutaway of the NPI sensor.

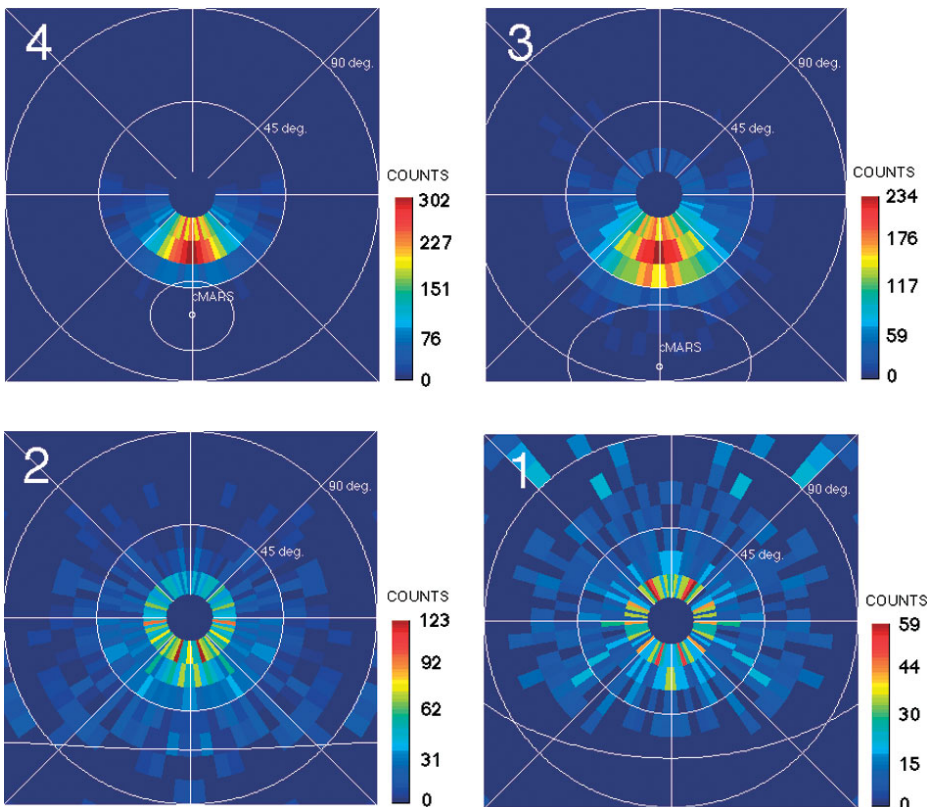
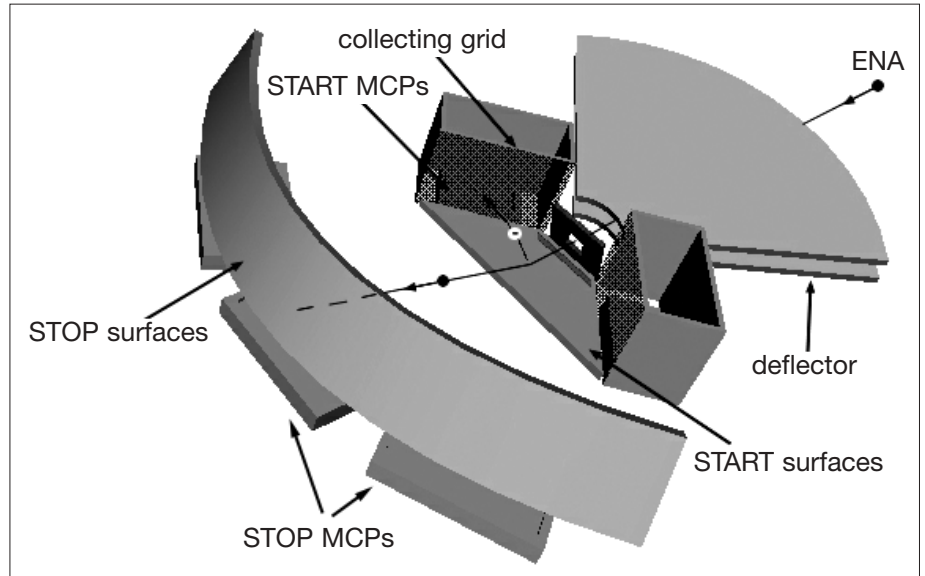


Fig. 8. ENA images expected from NPI for the locations along the Mars Express orbit specified in Fig. 2 (position 4 corresponds to the orbit apocentre). The images were generated assuming the instrument characteristics given in Table 2. The Sun is in the centre of the image. The solar wind ENAs coming from the Sun direction are not shown. The projection is similar to that in Fig. 3.

a star-like structure. This configuration allows the entering particles to experience multiple reflections and reach the MCP. NPI covers 4π in one instrument scan and produces an image of the ENA distribution in the form of an azimuth x elevation matrix. The direction vector of 32 elements can be read out once every $31.25 \mu\text{s}$. Two sectors centred around the spin axis and looking toward the spacecraft body are blocked to monitor the MCP assembly dark counts. This space is also used for the ELS sensor harness.

An important issue in designing the NPI was the target coating for suppressing UV photon fluxes, which produce the UV background in the measurements. NPI uses the same coating as in the PIPPI/Astrid and ASPERA-C experiments: DAG 213, a resin-based graphite dispersion. This is similar to Aquadag, which is a graphite dispersion in water. The coating demonstrated satisfactory performance in the PIPPI experiment

Fig. 9. NPD's principal components.



flown in the Earth's magnetosphere (C:son Brandt et al., 2000). Fig. 8 shows ENA images expected from NPI for the locations along the Mars Express orbit specified in Fig. 2.

2.4 Neutral Particle Detector (NPD)

The NPD contains two identical sensors, each a pinhole camera. Fig. 9 provides a conceptual view of one sensor. In each sensor, the charged particles, electrons and ions are removed by the deflection system, which consists of two 90° sectors separated by a 4.5 mm gap. In the normal operational mode, the 10 kV potential (± 5 kV) applied to the sectors results in a strong electric field that sweeps away all charged particles with energies up to 70 keV. The deflector also collimates the incoming beam in the elevation angle. The collimated ENA beam emerging from the 3.0x4.5 mm pinhole hits the START surface under the 15° grazing angle and causes secondary electron emission. By a system of collecting grids, the secondary electrons are transported to one of two MCP assemblies, giving the START signal for the TOF electronics. Depending on the azimuth angle, the collection efficiency varies from 80% to 95%. The incident ENAs are reflected from the START surface near-specularly. Since charge-state equilibrium is established during the interaction with the surface, the emerging beam contains both the neutral and ionised (positive and negative) components. To increase the total efficiency, no further separation by the charge is made. As proved by the ion tracing, there is very little disturbance to the reflected atomic ions leaving the START surface with energies above 80 eV, introduced by the START electron optics. Fig. 10 shows the results of electron ray-tracing in the START assembly electron optic.

Therefore, particles of all charge-states (negative, neutral and positive) will impact the second surface, the STOP surface, and again produce secondary electrons, which are detected by one of the three MCP assemblies giving the STOP signal. The TOF over a fixed distance of 8 cm defines the particle speed. The STOP MCPs also give the azimuthal direction. Since the secondary electron yield depends on mass for a given velocity, the pulse height distribution analysis of the STOP signals provides the estimation of ENA mass. Each event is stored in the array STOP MCP charge x TOF x direction. The content of the array is accumulated over the sampling time of 31.25 μ s. Fig. 11 shows one of the NPD Flight Model sensors.

The selection of the START and STOP surfaces was the most difficult part of NPD's development. Extensive studies were performed at the University of Bern

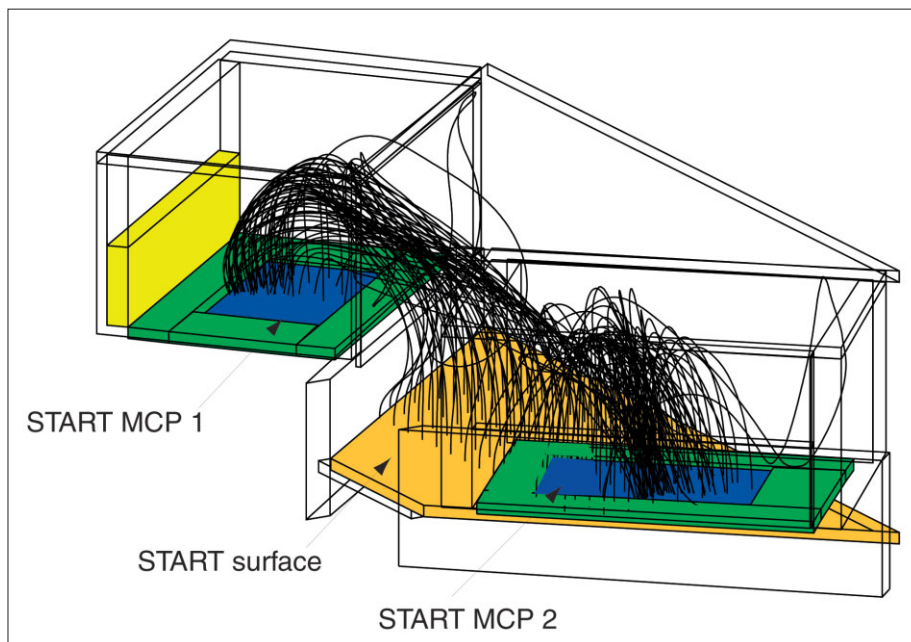


Fig. 10. The ray-tracing of the electron trajectories in the START assembly optics.

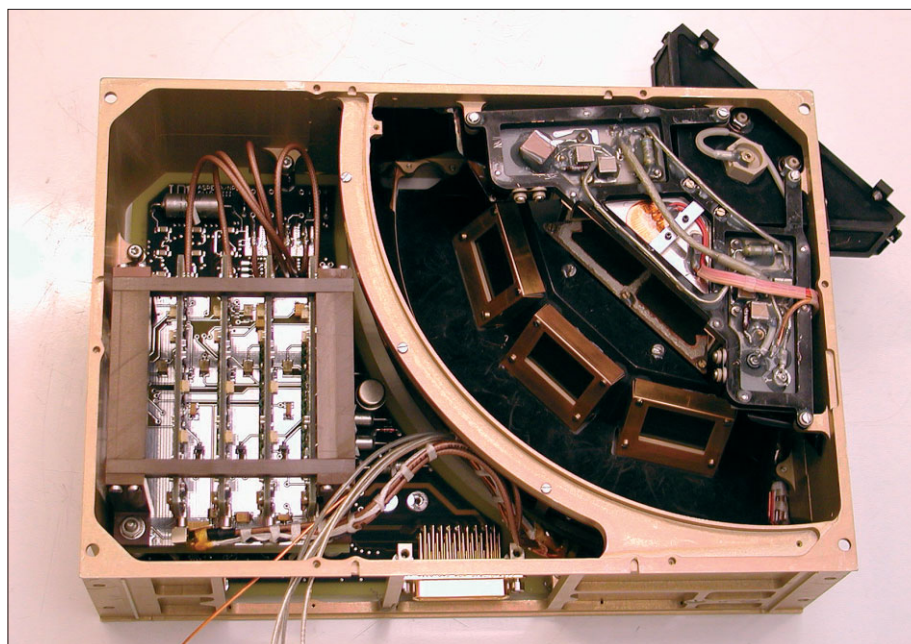


Fig. 11. Flight Model of the NPD sensor.

(Jans, 2000) and Brigham Young University (USA) to optimise the performance of the surfaces, which must satisfy a number of requirements: high secondary-electron yield, high UV absorption even at grazing angles, high particle reflection coefficient (START surface), low angular scattering of ions, and low photoelectron yield. For the START surface, a multi-layer coating composed of a thin layer of Cr_2O_3 covered by a thicker layer of MgF and topped with a thin layer of WO_2 was chosen. The coating is optimised for the absorption of the 121.4 nm line at the 15° incident angle. The reflection coefficient reached was about 30%, a factor of 2 lower than the uncoated surface. The coating is applied on a titanium substrate polished down to 100\AA roughness.

The STOP surface is graphite (roughness around 100 nm) covered by a MgO layer about 500 nm thick. This combination has a very high secondary electron yield, low

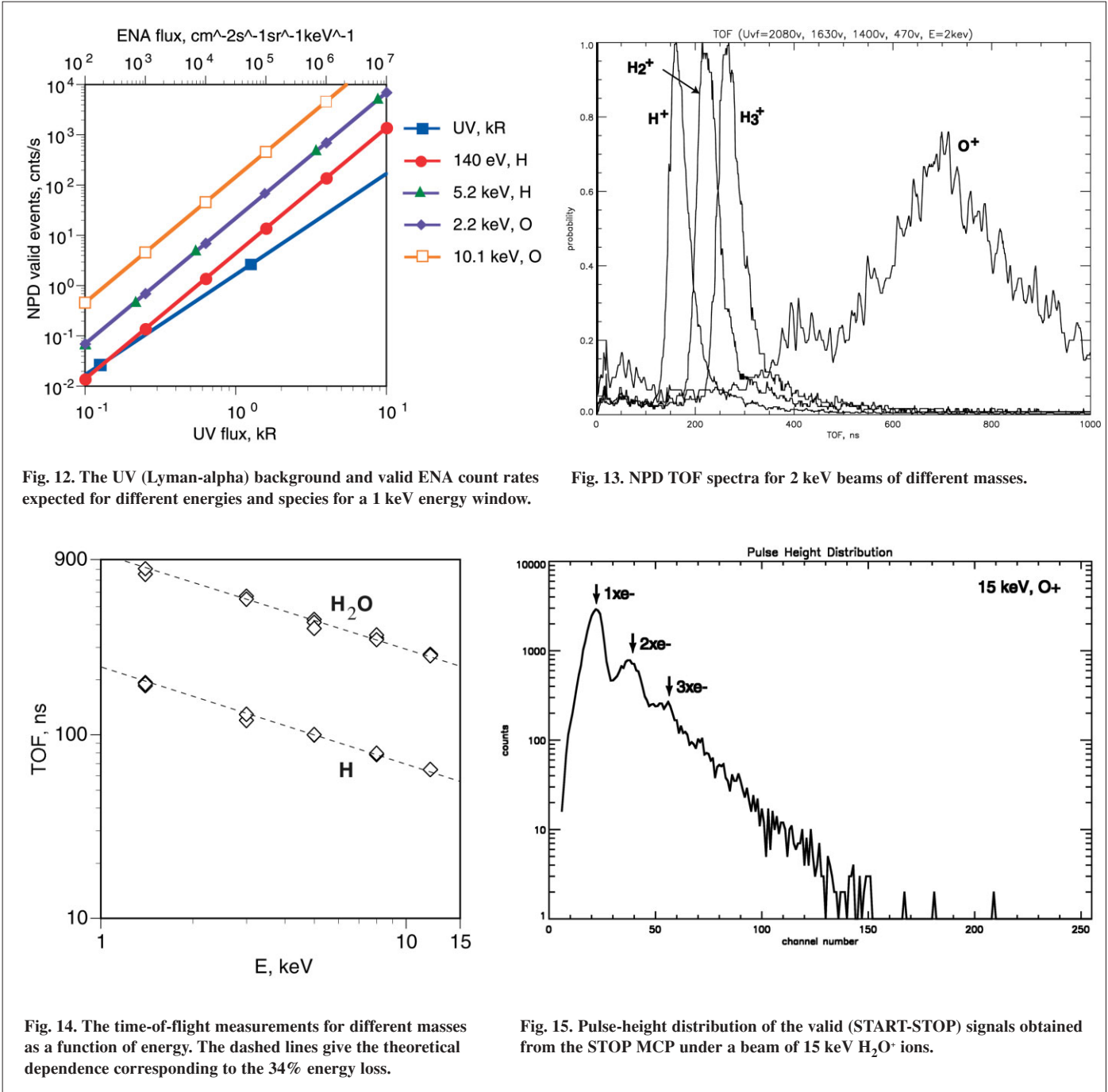


Fig. 12. The UV (Lyman-alpha) background and valid ENA count rates expected for different energies and species for a 1 keV energy window.

Fig. 13. NPD TOF spectra for 2 keV beams of different masses.

Fig. 14. The time-of-flight measurements for different masses as a function of energy. The dashed lines give the theoretical dependence corresponding to the 34% energy loss.

Fig. 15. Pulse-height distribution of the valid (START-STOP) signals obtained from the STOP MCP under a beam of 15 keV H₂O⁺ ions.

photoelectron yield and high UV absorption. Considerable effort was made to increase the stability of the MgO coating against moisture. It was established that polishing the graphite substantially improves the stability, and that possible increases in air humidity during storage and pre-launch operations do not present any problems for the surface performance. Both surfaces are stable and do not require special maintenance. Fig. 12 presents the expected count rates for different ENA and UV fluxes (Lyman- α) and a TOF window of 1.56 ms defined by the slowest (300 eV) oxygen atoms travelling the TOF distance. The valid count rates are given for different species and energies because of the secondary electron yield and reflection coefficient variations. An energy window of 1 keV is taken and the coefficients

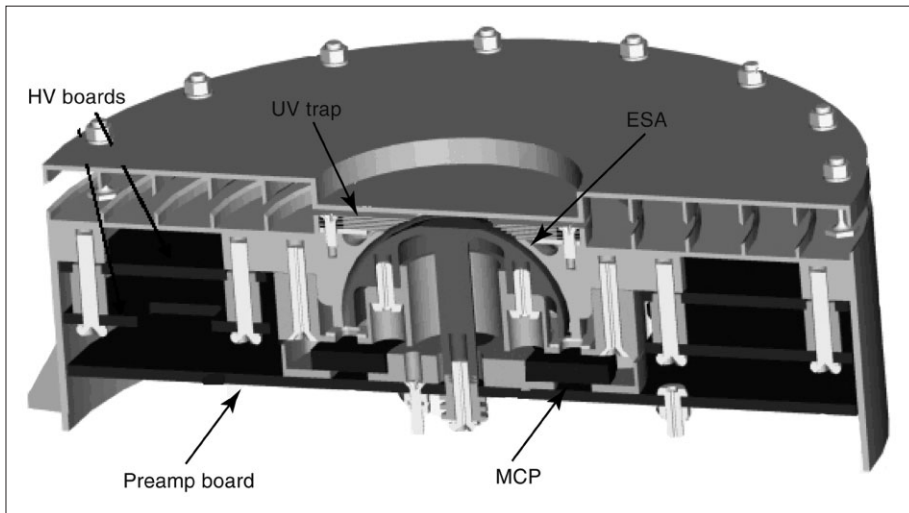


Fig. 16. The ELS sensor.

describing the interaction with the surface are assumed to be constant. In reality, of course, the instrument measures over the entire energy range 0.1-10 keV. Therefore, Fig. 12 gives count rates for a narrow (in energy terms) beam of oxygen and hydrogen atoms. The expected UV flux is about 4 kR close to the martian limb (Anderson, 1974); that gives fluxes, corresponding to a signal-to-noise ratio of 1, of $2 \times 10^5 \text{ cm}^{-2} \text{ s}^{-1} \text{ sr}^{-1} \text{ keV}^{-1}$ (H, 140 eV), $3 \times 10^4 \text{ cm}^{-2} \text{ s}^{-1} \text{ sr}^{-1} \text{ keV}^{-1}$ (H, O, few keV) and $4 \times 10^3 \text{ cm}^{-2} \text{ s}^{-1} \text{ sr}^{-1} \text{ keV}^{-1}$ (O, 10 keV).

The initial tests with the NPD technology model gave results fully corresponding to the specified performance. Fig. 13 shows TOF spectra for 2 keV beams of different masses. Fig. 14 summarises TOF measurements. The dashed lines show the theoretical dependence corresponding to the 34% energy loss in the START surface. The water molecules produced in the ion source break up during the impact but the residual components carry the same initial velocity corrected for the energy loss in the target. Fig. 14 shows that, within 1-10 keV, the TOF measurements give reliable mass identification. The other independent way of mass identification is based on the mass dependence of the number of electrons produced from the STOP surface. Fig. 15 shows a pulse-height distribution of the valid (START-STOP) signals obtained from the STOP MCP when a beam of 15 keV H_2O^+ ions was used. The different peaks correspond to different numbers of secondary electrons released from the STOP surface.

2.5 Electron Spectrometer (ELS)

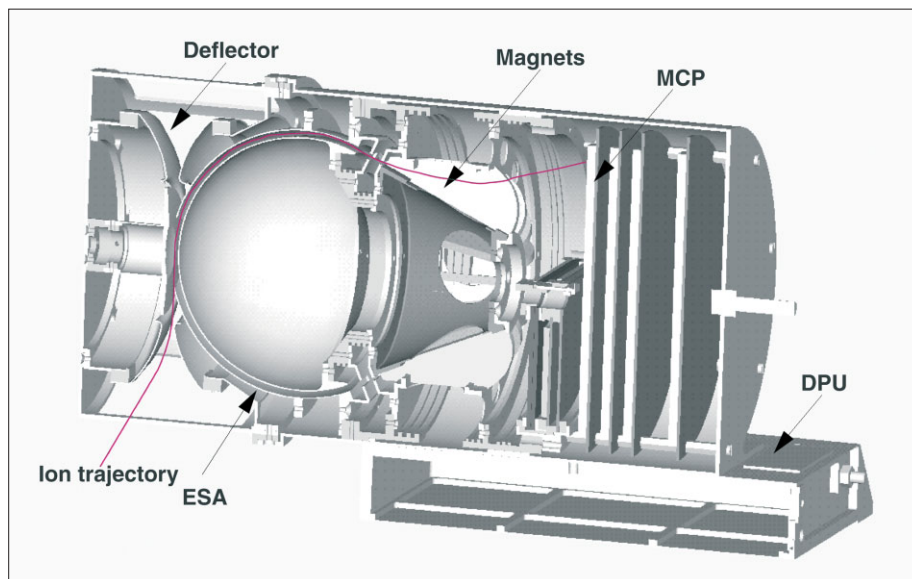
ELS represents a new generation of ultra-light, low-power, electron sensors (Fig. 16). It is formed by a spherical top-hat electrostatic analyser and a collimator system. Particles enter the aperture at any angle in the plane of incidence. Electrons are then deflected into the spectrometer by applying a positive voltage to the inner spherical electron deflection plate. The electrons hit an MCP after being filtered in energy by the analyser plates. The plates are stepped in voltage to achieve an energy spectrum.

Electrons with energies up to $20 \text{ keV}/q$ will be measured, with a maximum time resolution of one energy sweep per 4 s. There are 16 anodes behind the MCP, each anode defining a 22.5° sector and connected to a pre-amplifier. ELS is mounted on the ASPERA-3 scan platform, on top of the NPI sensor, so that the full 4π angular distribution of electrons is measured during each platform scan.

2.6 Ion Mass Analyser (IMA)

IMA (Fig. 17) is an improved version of the ion mass spectrographs TICS (Freja, 1992), IMIS (part of ASPERA-C/Mars-96, 1996) and IMI (Planet-B, 1998) (Norberg

Fig. 17. Cross-section view of the IMA sensor.



et al., 1998). It is a copy of the ICA instrument to be launched on Rosetta to Comet Wirtanen in 2003. Particles enter the analyser through an outer grid. Behind the grid is a deflection system to divert particles coming from between 45° and 135° with respect to the symmetry axis into the electrostatic analyser (ESA). Ions within a swept energy pass band pass the ESA. They are then deflected in a cylindrical magnetic field set up by permanent magnets. The field deflects lighter ions more than heavy ions away from the centre of the analyser. The ions finally hit an MCP and are detected by an anode system. Ions are simultaneously analysed for direction and mass per charge. The magnet assembly can be biased with respect to the ESA to post accelerate ions, enabling a selection of both mass range and mass resolution.

The electrons from the MCP are detected by an 'imaging' anode system. A system of 32 concentric rings behind the MCP measures the radial impact position (representing ion mass) and 16 sector anodes measure the azimuthal impact position (representing ion entrance angle). The read-out system is based on discrete pre-amplifiers. Six MOCAD (Monolithic Octal Charge Amplifier/Pulse Discriminator) chips provide 48 independent channels, 32 rings and 16 sectors. Each chip contains eight channels including a charge-sensitive pre-amplifier, shaper and discriminator. The transistor-transistor logic (TTL) outputs are fed to a field-programmable gate array FPGA device for decoding, addressing and coincidence analysis. Fig. 18 demonstrates the achieved mass resolution at 6 keV ion energy.

3. The Team

The ASPERA-3 experiment team is a large consortium that includes 15 groups from 10 countries in Europe, the USA and Japan. Table 3 shows the primary hardware responsibilities of the different groups.

References

- Acuna, M.H., Connerney, J.E.P., Wasilewski, P., Lin, R.P., Anderson, K.A., Carlson, C.W., McFadden, J., Curtis, D.W., Mitchell, D., Reme, H., Mazelle, C., Sauvaud, J.A., d'Uston, C., Cros, A., Medale, J.L., Bauer, S.J., Cloutier, P., Mayhew, M., Winterhalter, D. & Ness, N.F. (1998). Magnetic Field and Plasma Observations at Mars: Initial Results of the Mars Global Surveyor Mission. *Science* **279**, 1676.
- Anderson, D.E. (1974). Mariner 6, 7, and 9 Ultraviolet Spectrometer: Analysis of Hydrogen Lyman alpha Data. *J. Geophys. Res.* **79**, 1513-1518.

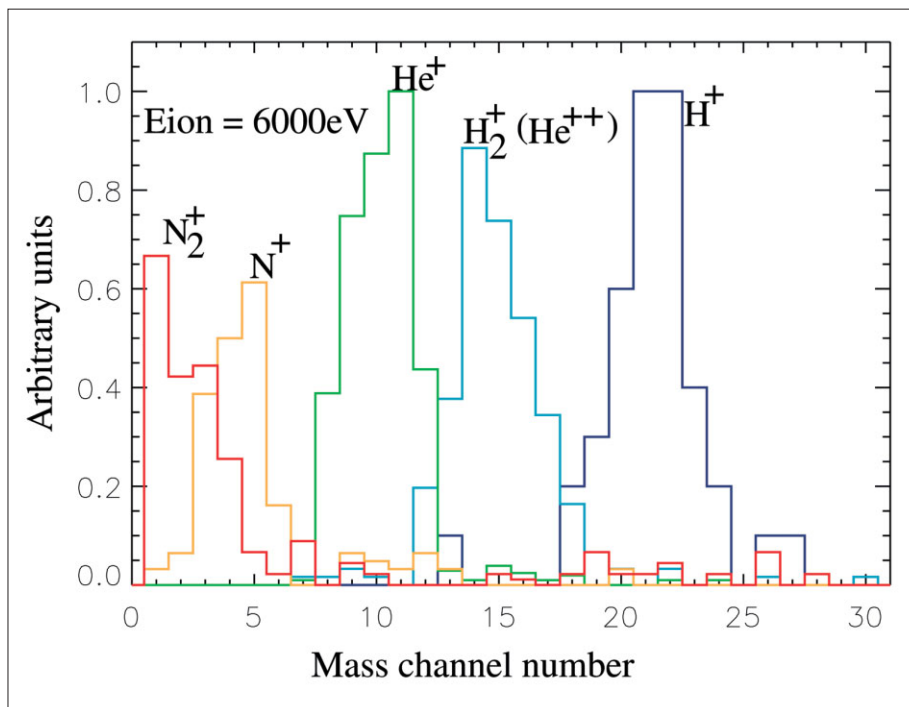


Fig. 18. IMA mass resolution at 6 keV.

Table 3. ASPERA-3 groups and primary hardware responsibilities.

<i>Species</i>	<i>Scientific objective</i>
Swedish Institute of Space Physics, Kiruna, S	PI-institute, NPI, NPD, IMA, scanner
Institute of Space and Astronautical Science, Sagamichara, JPN	Collaboration with Nozomi, NPI calibrations
University of Bern, Physikalisches Institut, CH	NPD surfaces, NPD mechanics
Instituto di Fisica dello Spazio Interplanetari, Rome, I	EGSE, NPI mechanics, NPD electronics
Mullard Space Science Laboratory, UCL, UK	ELS calibrations
University of Arizona, Tucson, Arizona, USA	START surface, NPD UV calibrations
Space Research Institute, Moscow, Russia	NPD design
Southwest Research Institute, San Antonio, USA	ELS, IMA imaging detector
Rutherford Appleton Laboratory, UK	NPD MCPs
Finnish Meteorological Institute, Helsinki, FIN	DPU, theory
Space Physics Research Lab/University of Michigan, Ann Arbor, Michigan, USA	Theory
Max-Planck-Institut für Aeronomie, Katlenburg-Lindau, D	NPD electronics
Space Science Lab/University of California in Berkeley, Berkeley, California USA	Theory
Space Technology Ltd., National University of Ireland, IRL	Hardware support
Applied Physics Lab/Johns Hopkins University, Laurel, Maryland, USA	Theory
Centre d'Etude Spatiale des Rayonnements, Toulouse, F	NPI MCPs, IMA calibrations, DC/DC board, scanner drivers

- Barabash, S., Lundin, R., Zarnowiecki, T. & Grzedzielski, S. (1995). Diagnostic of Energetic Neutral Particles at Mars by the ASPERA-C Instrument for the Mars-96 Mission. *Adv. Space Res.* **16**, (4)81.
- Barabash, S. (1995). Satellite Observations of the Plasma-Neutral Coupling near Mars and the Earth. *IRF Scientific Report* 228.
- Barabash, S., Holmström, M., Lukyanov, A. & Kallio, E. (2002). Energetic Neutral Atoms at Mars IV: Imaging of Planetary Oxygen. *J. Geophys. Res.* **107**(A10), doi: 10.1029/2001JA000326.
- Brecht, S.H. (1997). Solar Wind Proton Deposition into the Martian Atmosphere. *J. Geophys. Res.* **102**, 11,287.
- C:son Brandt, P., Barabash, S., Wilson, G.R., Roelof, E.C. & Chase, C.J. (2000). Energetic Neutral Atom Imaging at Low (< 10 keV) Energies from Astrid: Observations and Simulations. *J. Atmos. & Solar Terrestrial Phys* **62**, 901-910.
- Dornheim, M.A. (1997). Mars Atmosphere Thicker than Expected. *Av. Week & Space Tech.* (29 September), 36.
- Dubinin, E., Sauer, K., Lundin, R., Norberg, O., Trotignon, J.-G., Schwingschuh, K., Delva, M. & Riedler, W. (1996). Plasma Characteristics of the Boundary Layer in the Martian Magnetosphere. *J. Geophys. Res.* **101**, 27,061.
- Holmström, M., Barabash, S. & Kallio, E. (2002). Energetic Neutral Atoms at Mars I: Imaging of Solar Wind Protons. *J. Geophys. Res.* **107**(A10), doi: 10.1029/2001JA000325.
- Jans, S. (2000). *Ionization of Energetic Neutral Atoms for Application in Space Instrumentation*, Diplomarbeit der Philosophisch-naturwissenschaftlichen Fakultät der Universität Bern, CH.
- Farmer, C.B., Davies, D.W., Holland, A.L., LaPorte, D.D. & Downs, P.E. (1977). Mars: Water Vapour Observations from the Viking Orbiters. *J. Geophys. Res.* **82**, 4225.
- Kallio, E. & Barabash, S. (2000). On the Elastic and Inelastic Collisions between the Precipitating Energetic Hydrogen Atoms and the Martian Atmospheric Neutrals. *J. Geophys. Res.* **105**, 24973-24996.
- Kallio, E. & Barabash, S. (2001). Atmospheric Effects of Precipitating Energetic Hydrogen Atoms to the Martian Atmosphere. *J. Geophys. Res.* **106**, 165-177.
- Kallio, E. & Janhunen, P. (2001). Atmospheric Effects of Proton Precipitation in the Martian Atmosphere and its Connection to the Mars-Solar Wind Interaction. *J. Geophys. Res.* **106**, 5617.
- Kallio, E. & Koskinen, H. (1999). A Test Particle Simulation of the Motion of Oxygen Ions and Solar Wind Protons near Mars. *J. Geophys. Res.* **104**, 557-579.
- Kallio, E., Luhmann, J.G. & Barabash, S. (1997). Charge Exchange near Mars: The Solar Wind Absorption and Energetic Neutral Atom Production. *J. Geophys. Res.* **102**, 22,183.
- Lichtenegger, H., Lammer, H. & Stumptner, W. (2002). Energetic Neutral Atoms at Mars III: Flux and Energy Distribution of Planetary Energetic H Atoms. *J. Geophys. Res.* **107**(A10), doi: 10.1029/2001JA000326.
- Luhmann, J.G. & Bauer, S.J. (1992). Solar Wind Effects on Atmospheric Evolution at Venus and Mars. In *Venus and Mars: Atmospheres, Ionospheres, and Solar Wind Interactions*, AGU Monograph, **66**, 417-430
- Luhmann, J.G. & Kozyra, J.U. (1991). Dayside Pickup Oxygen Ion Precipitation at Venus and Mars: Spatial Distributions, Energy Deposition and Consequences. *J. Geophys. Res.* **96**, 5457.
- Luhmann, J.G., Johnson, R.E. & Zhang, M.H.G. (1992). Evolutionary Impact of Sputtering of the Martian Atmosphere by O⁺ Pickup Ions. *Geophys. Res. Lett.* **19**, 2151.
- Lundin, R., Zakharov, A., Pellinen, R., Borg, H., Hultqvist, B., Pissarenko, N., Dubinin, E.M., Barabash, S.W., Liede, I. & Koskinen, H. (1989). First Measurements of the Ionospheric Plasma Escape from Mars. *Nature* **341**, 609.
- Lundin, R., Dubinin, E., Koskinen, H., Norberg, O., Pissarenko, N. & Barabash, S.

- (1991). On the Momentum Transfer of the Solar Wind to the Martian Topside Ionosphere. *Geophys. Res. Lett.* **18**, 1059.
- Lundin, R., Dubinin, E., Barabash, S. & Norberg, O. (1993). ASPERA Observations of Martian Magnetospheric Boundaries. In *Plasma Environments of Non-magnetic Planets* (Ed. T.I. Gombosi), Pergamon Press, UK, p311.
- McKay, C.P. & Stoker, C.R. (1989). The Early Environment and its Evolution on Mars: Implications for Life. *Rev. of Geophys.* **27**, 189.
- Mura, A., Milillo, A., Orsini, S., Kallio, E. & Barabash, S. (2002). Energetic Neutral Atoms at Mars II: Energetic Neutral Atom Production near Phobos. *J. Geophys. Res.* **107**(A10), doi: 10.1029/2001JA000328.
- Norberg, O., Winningham, J.D., Lauche, H., Keith, W., Puccio, W., Olsen, J., Lundin, K. & Scherrer, J. (2001). The MEDUSA Electron and Ion Spectrometer and the PIA Ultraviolet Photometers on Astrid-2. *Ann. Geophys.* **19**, 593.
- Norberg, O., Yamauchi, M., Lundin, R., Olsen, S., Borg, H., Barabash, S., Hirahara, M., Mukai, T. & Hayakawa, H. (1998). The Ion Mass Imager on the Planet-B Spacecraft. *Earth, Planets and Space* **50**, 199-205.
- Perez-de-Tejada, H. (1992). Solar Wind Erosion of the Mars Early Atmosphere. *J. Geophys. Res.* **97**, 3159.
- Roelof, E.C. & Skinner, A.J. (2000). Extraction of Ion Distributions from Magnetospheric and EUV Images. *Space Sci. Rev.* **91**, 437-459.
- Verigin, M., Gringauz, K.I., Kotova, G.A., Shutte, N.M., Rosenbauer, H., Livi, S., Richter, A.K., Riedler, W., Schwingenschuh, K. & Szegö, K. (1991). On the Problem of the Martian Atmosphere Dissipation: PHOBOS 2 TAUS Spectrometer Results. *J. Geophys. Res.* **96**, 19,315-19,320.
- Wurz, P. (2000). Detection of Energetic Neutral Particles. In *The Outer Heliosphere: Beyond the Planets* (Eds. K. Scherer, H. Fichtner & E. Marsch), Copernicus Gesellschaft, Katlenburg-Lindau, Germany, pp251-288.

Acknowledgment

The authors are grateful to A. Balogh and C. Carr (both Imperial College, London, UK) for providing the IEEE-1355 link chip developed for the Rosetta mission.